Hot Deformation Behaviour of EN30B Forged Steels in the Presence of Non-Metallic Inclusions

Vasundhara Singh[a], Prakash Srirangam[b], Debalay Chakrabarti[a], and

Gour Gopal Roy[a*]

[a] *Department of Metallurgical and Materials Engineering,*

Indian Institute of Technology Kharagpur,

Kharagpur, 721302, India

[b] *Warwick Manufacturing Group,*

University of Warwick, Coventry,

CV4 7AL, UK

**Corresponding author:* bravevasu25@gmail.com

Revision 1

Submitted to

Journals of Materials Engineering and Performance

September, 2022

ABSTRACT

The hot deformation behaviour of EN30B steel in the presence of inclusion has been studied using the Gleeble® simulator 3800. The Processing maps are developed to identify the range of parameters (temperature, strain, and strain rate) for a safe deformation zone. Safe deformation zones are identified at various strain levels. The safe zone is found to lie in the high temperatures (1110 to 1150°C) and high strain rates (6 to10 s^{-1}) at lower deformation (true strain = 0.4), which subsequently moves to low strain rates (0.1 to 0.8/s) and wide temperature regime (1000 to 1150^{o}C) at higher strain labels (0.6 to 1.2). With the shear band generation, there is a competition between favourable and unfavourable microstructural evolution, which shifts the safe zone at various strain levels. The evolution of inclusions and cracks at different strain rates and temperatures are examined using SEM and correlated with the processing maps. Cracks were initiated at compound inclusions and propagated in the lower temperatures and higher strain rate regimes, identified as the unstable plastic deformation zone in the processing map. An estimated higher volume fraction of the dynamically recrystallized grains in the safe deformation zone attributed to arresting the cracks.

Keywords: - EN30B steel, Non-metallic inclusions, Gleeble® simulation, Cracks, Processing maps.

1. Introduction

Medium carbon low alloy (MCLA) Ni–Cr–Mo steels have been a centre of attraction for many researchers in the last few decades. Several studies have been conducted on MCLA steels due to their excellent balance of strength, toughness, and wear resistance. British standards grades like EN30B, EN18, EN19 (AISI 4140), EN24 (AISI 4340), EN30B, 34CrMo4, 42CrMo belong to this category of steels. EN grade Ni–Cr–Mo steels find application in machine part members, gears, and shafts due to their high hardenability, good tensile strength, and toughness, which could be tailored by proper heat treatment (**Ref 1**). EN30B steel shows a tensile strength of more than 1000 MPa with 13% ductility. The evolution of stress and strain behaviour during hot deformation of EN30B steel in the presence of inclusion is an important study not reported so far.

Several authors studied the hot deformation behaviour of 42CrMo MCLA steel. Based on FEM simulation, **Lin et al.** reported that the evolution of strain and DRX (dynamic recrystallized) grains were inhomogeneous in the deformed sample, the extent of which decreased with an increase in strain rate (**Ref. 2, 3**). Similarly, Chadha et al. (**Ref. 4**) calculated more uniform temperature distribution at a higher strain rate during hot deformation of as-cast 42CrMo steel. Subsequently, Lin et al. (**Ref. 5**) developed a processing map that identified a safe zone of hot deformation for 42CrMo steel in a temperature range of 1050-1150˚C and a wide strain rate range of 0.01 to 3/s. **Chen et al.** (**Ref. 6**) showed that refined austenite grains favoured DRX grain formation during the hot compression of 42CrMo steel. **Quan et al.** (**Ref. 7**) showed that the microstructure became more refined at higher strain rate and the DRX-refined average grain size increased rapidly beyond 1273K.

Few hot deformation studies have also been concentrated on 34CrMo4 MCLA steel. **S V Sajadifar et al**. **(Ref. 8)** estimated hot deformation activation energy at 491 kJ /mol. Based on theoretical and experimental study, they also showed that the flow curves exhibited single or multiple peaks before reaching a steady state **(Ref. 9)**. **Xiao et al. (Ref. 10)** identified the safe zone of hot deformation in the temperature range of 850 to 900 °C and strain rates in the range of 10 to 20 s^{-1} for 34CrMo4 steel.

Several studies have been carried out on several other medium carbon alloy steel, which are grouped in this paragraph. **M.I.Mehta et al.** (**Ref. 11**) studied the flow behaviour of rotor grade steel 28CrMoNiV59 and showed that in an intermediate temperature range (~200 °C to 350 °C), flow stress increased with temperature, attributed to the uniform precipitation of fine

carbide particles. **A. Momeni et al.** (**Ref. 12**) estimated hot deformation activation energy at 435 kJ/mol for VCN200 medium carbon low alloy steel. **M. Mirzaee et al.** (**Ref. 13**) reported that for hot deformation of 26NiCrMoV steel, predicted flow stress produced a significant deviation from experimental data below 1000^{o}C, attributed to dynamic precipitation. **Ferdowsi et al.** (**Ref. 14**) showed that for medium carbon micro-alloyed Si-Mn-V-Cr steel, the true strain required to get a certain volume fraction of DRX increased with a decrease in deformation temperature but decreased with an increase in strain rate. **F. Zhang et al.** (**Ref. 15**) showed that for medium carbon Si-Mn-Cr steel, grain size decreased, hardness passed through peak, and impact toughness monotonically increased with an increase in deformation. **G.L.Wu. et al.** (**Ref. 16**) reported that an unstable region belonged to the temperature range of 1010-1100°C when strain rates exceeded 0.78 s^{-1} for Nb-Ti micro-alloyed steel**. M. Sadeghi et al.** (**Ref. 17**) reported that for Mn-Ni-Cr alloy steel, a remarkable decrease in flow stress in the temperature range from 700 to 750^{o}C was attributed to the dissolution of Mn_3C and forming a single-phase solid solution.

S. V. Sajadifar et al. (**Ref. 18**) estimated the activation energy of hot deformation of automobile grade 4340 steel at 427 kJ/mol. They also reported that the strain rate sensitivity of the alloy increased from 0.106 at 900°C to 0.149 at 1200°C, improving workability at higher temperatures. **Yang et al.** (**Ref. 19**) reported a higher fraction of DRX grains at higher temperatures and lower strain rates for BT25y alloy. **Sun et al.** (**Ref. 20**) identified the safe zone of deformation for Fe-30Mn-10Al-1C low-density steel in the temperature range of 975-1100^{o}C and strain rate range of 0.01 to1s^{-1} with the efficiency of powder dissipation in the range 36 to 64%.

Lin et al. (Ref. 21) studied the hot deformation behavior of Ni-based superalloys by EBSD analysis and demonstrated that low angle grain boundaries (LAGB) decreased with an increase in deformation temperature or decrease in strain rate, which was linked to an increase in DRX. The fraction of LAGB increased rapidly at a relatively small deformation degree and progressively decreased with an increase in DRX. **M. S. Chen (Ref. 22)** studied the effect of stepped strain rate on DRX of solution-treated and aged Ni-based superalloy. They showed that under stepped strain rate deformation, DRX decelerated for solution treated sample and accelerated for the aged sample. Z. **Chen et al. (Ref. 23)** developed a model to predict the flow behaviour of aged Ni-based superalloys. They demonstrated that an enhanced initial delta phase increased dynamic recrystallization and refined grains.

Several studies were also reported on the inclusion behaviour of steel during deformation. During hot forging of 30Cr4Ni2MoV ingot, **Zhao et al. (Ref. 24)** reported that when stress was applied parallel to plastic sulphide inclusions, more extensive fault formed in the overlapped region of strains around adjacent inclusions. They further reported that in brittle compound inclusion containing several fragmented particles, stress developed at both sides of the particles, and cracks initiated and propagated, connecting each other. **Z. Xiao et al. (Ref. 25)** showed that 35CrMo steel deformed at high temperatures or low strain rates failed due to the coalescence of numerous voids in the recrystallized grains. In contrast, the fracture was attributed to the crack initiation at inclusions at high strain rates or low temperatures. Based on FEM simulation, **N. K. Kanoje et al. (Ref. 26)** studied the inclusion response during railway wheel failure and reported that the stress intensity factor at the alumina inclusion crack tip was higher when inclusion was laid parallel to the rolling direction, but for MnS inclusion, it was higher for all crack orientations, indicating that MnS inclusions were more likely to cause cracks. Based on modelling and experimental studies, **Qi et al**. **(Ref. 27)** showed that the deformation of plastic inclusion was compatible with the matrix, while harder inclusion rarely deformed and initiated a conical crack in the matrix. **Singh et al. (Ref. 28)** reported that non-deformable and incoherent alumina inclusions acted as a crack initiator in the forged steels.

From the above literature survey, it is evident that several studies reported on the deformation behaviour of various materials, including MCLA. They mainly reported on developing the constitutive equations for flow stress, the kinetic equation for DRX, the estimation of activation energy of deformation, and the processing map identifying the safe zone of deformation in the two-dimensional domain of temperature and strain rates. However, to our knowledge, no literature reported the hot deformation behaviour of EN30B steel (medium carbon Ni-Cr-Mo low alloy steel). Besides, the presence of inclusions also influences the dynamic response of the material under hot deformation and the evolution of the safe deformation zone. Although few studies reported the mechanism of fault formation in the presence of soft and hard inclusions, a study correlating the evolution of inclusion with processing map has rarely been reported for medium carbon low alloy steel (MCLA), especially for EN30B steel.

In the present study, Gleeble® physical simulation is carried out on EN30B steel. Experimental flow stresses are analysed to develop processing maps by superimposing instability maps and power dissipation maps. The present study identifies the safe deformation zones during the hot compression of EN30B steel in the presence of inclusions. The evolution of inclusions and

microstructure are correlated with the processing map, and the generation of cracks is explained.

2. Experiments

2.1. Materials

The chemical composition of the as-cast ingot of EN30B steel, received from Heavy Engineering Corporation, India, as detected by optical emission spectroscopy, is shown in Table 1. The ingot was treated with calcium injection for inclusion modification during upstream processing. The ingot was verified free of any cracks in the ultra-sonic inspection.

Table 1: Chemical composition of EN30B steel

Elements	C	Mn	Si	S	P	Cr	Ni	Mo	Al	Ca
Wt. %	0.29	0.488	0.24	0.009	0.015	1.26	4.2	0.25	0.013	0.0015

2.2. Experimental Procedure

A specific volume of material ($15 \times 15 \times 10$ cm^3) was cut from the center of a rectangular piece of cast ingot. Around 30 cylindrical samples, each of 8 mm diameter and 12 mm height, were prepared for thermo-mechanical simulation in Gleeble® 3800 **(Ref 29)**. A 0.2 mm thick tantalum foil was used between the specimen and the anvils to act as a spacer and lubricant, reducing the friction between the specimen and the die. Isothermal compression test was performed at three temperatures (950/1050/1150˚C), three strain rates (0.1, 1, 10/s), and up to 70% deformation. Standard nickel paste was used to keep the foils in place.

Considering the EN30B steel composition (Table 1), the austenite transformation start and end temperatures during heating (Ac1 = 670˚C and Ac3 = 755˚C, respectively) and ferrite transformation start and end temperatures during cooling (Ar1 = 621˚C and Ar3 = 743˚C, respectively) are predicted from the equations **(Ref 30-31)**. These temperatures are expected to vary to a certain extent depending on the heating and cooling rates. The deformation temperatures (≥ 950˚C) are much above the predicted transformation temperatures; hence, the deformation is expected to be performed in the single-phase austenite domain. The recrystallization stop temperature (TNR), as predicted from the equation **(Ref 32)**, is 941˚C. Hence, recrystallization is also expected to happen at the deformation temperatures of interest. The BS and MS Temperatures, as predicted from Andrew's equations **(Ref 30),** are 443˚C and

310˚C, respectively. Due to considerably high carbon, nickel, and chromium, the steel is expected to bear high hardenability compared to low-carbon, low-alloy steels.

In Gleeble® simulation, the samples were heated at a rate of 20˚C/s (typical to industrial processing) up to three different temperatures (950 / 1050 / 1150˚C) and soaked for 2 minutes **(Ref 33)** and water-quenched**.** The photographs of the sample before and after deformation are shown in Figures 1(b), respectively. The deformed samples were cut on longitudinal sections (i.e., cut parallel to compression direction), as shown in Figure 1(b). Samples were prepared using standard polishing methods for microstructural examination, and images were captured in unetched conditions to study the inclusions and cracks. The size of inclusions was measured using ImageJ software. A significant material has been studied, covering at least 100 inclusions at each processing condition.

Electron backscattered diffraction (EBSD) was carried out to understand microstructure evolution at various deformation temperatures and strain rates. Some optical micrographs etched with picric acid were developed. These micrographs revealed the prior austenite grains and their recrystallization behavior (Ref 34).

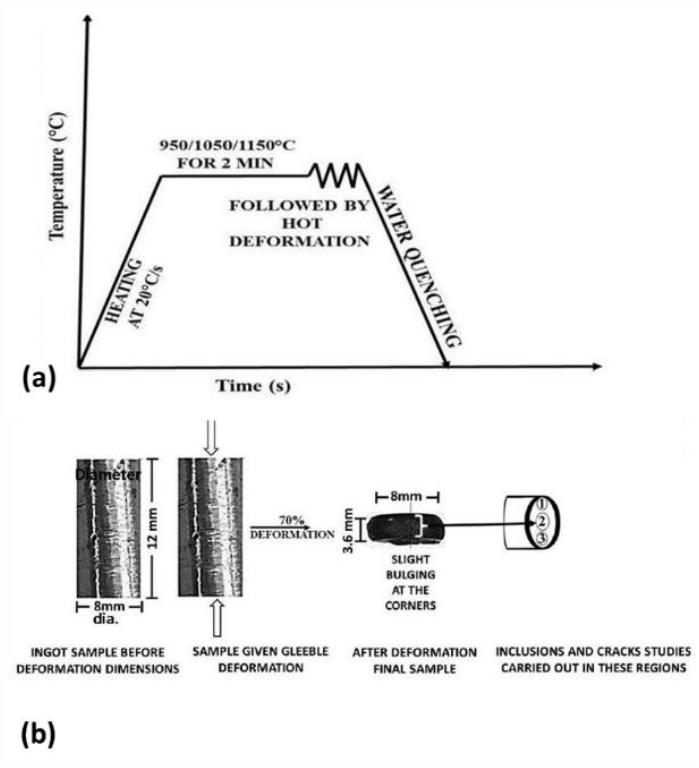

Figure 1: (a) Thermal cycle used in the Gleeble® simulation, and (b) sampling

3. Results and Discussion

3.1. Inclusion analysis of steel sample before the thermo-mechanical simulation

Micrographs of the calcium-treated unetched samples were obtained by optical and electron microscope. The inclusions' size, shape, morphology, and composition were studied before the hot-deformation simulation. Figure 2(a) shows the optical micrograph that depicts numerous inclusions (some of them in clusters) on the sample's surface. Subsequently, the inclusions were observed at higher magnifications, as shown in Figure 2(b - f). Figure 2(c) shows the clustering of inclusions. Inclusions were mainly, MnS and Al_2O_3. The size of Al_2O_3 inclusions was in the range of 10-20 μm. In contrast, the size of MnS inclusions was in the range of 20-40 μm.

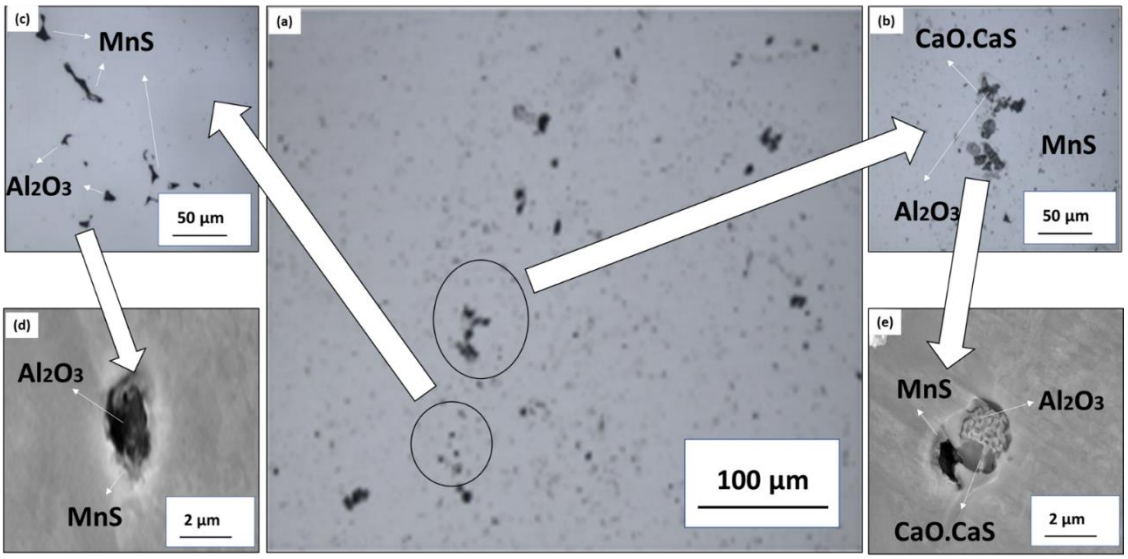

Figure 2: (a) shows the optical microscopy images of the EN30B steel, (b), (c), (d), (e) depict the SEM images at different magnifications, before thermo-mechanical simulation.

Although it was a calcium-treated sample, no significant amount of calcium aluminate inclusions was recorded in the EDS result. However, small clusters appeared at some places, where complex inclusions with CaO. CaS appears as an outlier of Al_2O_3 inclusions (Fig. 2(d),(e)). There were no visible cracks in the sample before the thermo-mechanical simulation.

3.2.True stress strain curve from Thermo-mechanical simulation

Figure 3 depicts the true stress-true strain curves of the hot compression test of EN30B steel at 70 % deformation with varying temperature and strain rates. Figure 3(a), (b), and (c) represent the material flow behaviour at different temperatures for strain rates of 0.1, 1.0, and 10.0/s,

respectively. The figure depicts that peak stress increases with an increase in strain rate and decreases with increasing temperature.

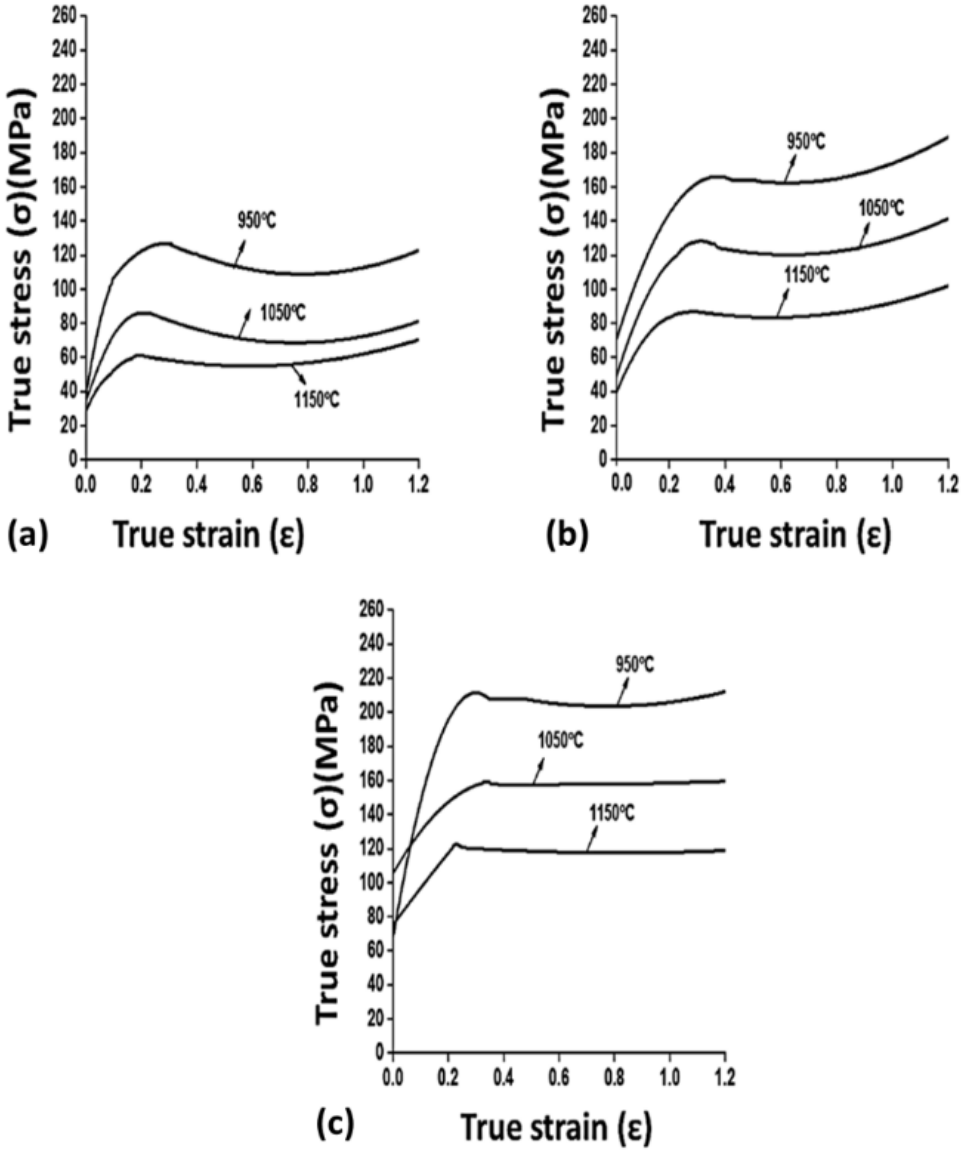

Figure 3: The Gleeble® generated true stress strain curves for 70 % deformation at different forging temperatures and at strain rates a) 0.1 /s, e) 1.0 /s and f) 10.0 /s

It may be noted that at low strain values, flow stress increases steeply (due to work hardening). It follows a decrease in steepness due to softening by dynamic recrystallization (DRX) at a critical stress (σ_c) until it reaches the peak stress. It is illustrated schematically in figure 4. The solid line in Figure 4 (a) represents the curve that could be expected in the absence of DRX. The plateau of this solid curve represents the saturation stress (σ_s). As shown by a dotted curve, the deviation at critical stress represents the evolved flow behaviour in dynamic softening

during the material's hot compression. Following the dotted line beyond the critical stress, the work hardening rate dominates over DRX up to peak stress. After that, DRX dominates over the work hardening, and flow stress starts to fall and finally flattens off with steady-state stress (σ_{ss}). From Fig. 3, it may be noted that in EN30B steel, after attaining the plateau, i.e., a steady-state stress level (σ_{ss}), the flow stress increased again with strain, at a high strain level (from 0.8 to 1.2). Such an increase in flow stress at large strain values can be attributed to friction at large deformation **(Ref 20)**. The friction at the specimen-platen interface reduces the flowability of the material adjacent to the interface. At high strain levels, as the specimen thickness reduces, the interface friction effect becomes significant **(Ref 35)**. The friction at the metal/platen interface could not be avoided entirely, despite using lubricant.

The variation in the work hardening parameter (θ), which defines the rate of change of stress with strain (slope of the stress-strain curve), when plotted against stress, is shown schematically in Figure 4 (b). The curve passes through three stages. In the 1st stage, θ is positive and decreases with an increase in stress, and the decrease in θ decelerates with an increase in stress until critical stress is reached where DRX starts (stage 2 starts). During the second stage, work-hardening dominates over DRX, and θ falls sharply till the flow stress attains peak stress (σ_p) when work hardening and DRX balance each other, and θ becomes 0. In the third stage, θ becomes negative when DRX dominates over work-hardening. First, it decreases and then increases until flow stress attains the steady-state stress (σ_{ss}) again at θ = 0 at comparatively lower stress than peak stress when the material deforms without further hardening.

This curve also yields saturation stress (σ_s). The value of σ_s is obtained by taking a tangent on the work-hardening curve (θ vs. σ) at a critical stress (when the curve just takes a turn) and extrapolating it to a stress value at θ equal to zero. The σ_c can also be obtained from the figure, but it could be derived more meaningfully at a stress value corresponding to the inflection point or minimum value of the – (dθ/dσ) vs. σ plot **(Ref 36)**. Dynamic recrystallization behaviour is predominantly recorded for all deformation conditions in the present case and discussed in table 2 under section 2.5.

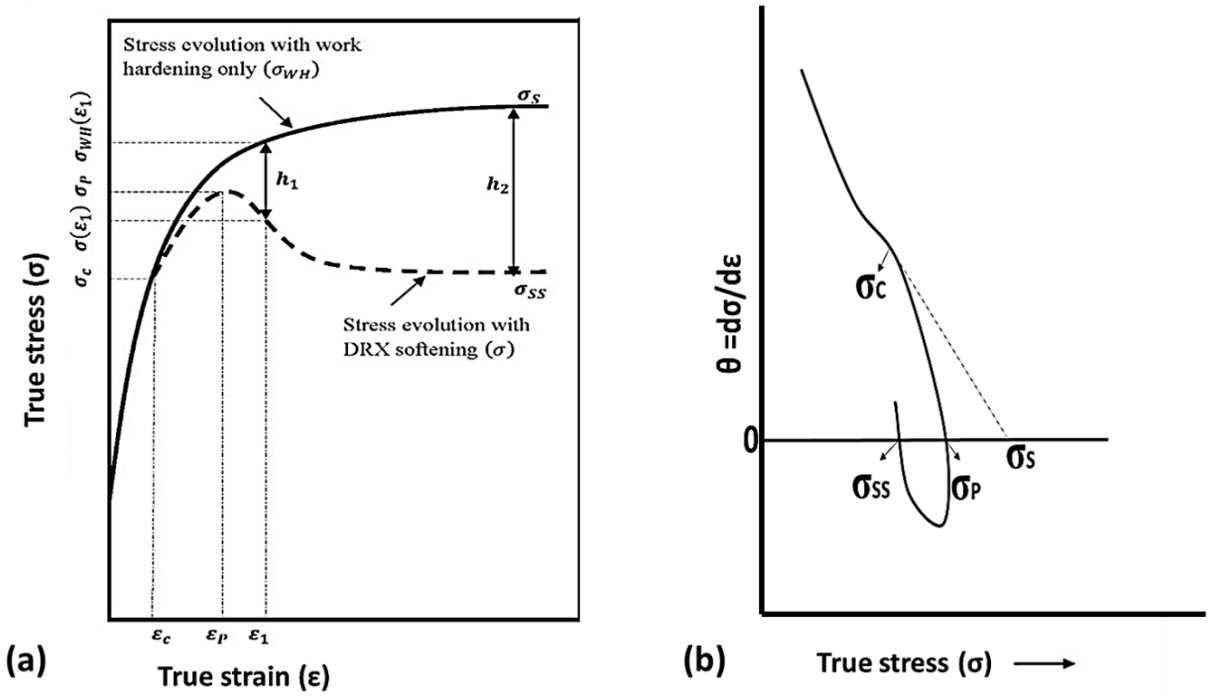

Figure 4: Schematics of (a) stress strain curve representing various flow stresses with and without DRX, b) work hardening curve (Ref 37).

3.3. Determination of volume fraction of dynamically recrystallized grains under different hot deformation conditions

The volume fraction of dynamic recrystallization (X_{DRX}) is calculated using equation 1 **(Ref 19, 36),** where stress values and magnitudes of a and b are depicted in Figure 4. σ represents the flow stress during hot deformation and σ_{WH} represents the hypothetical flow stress in the absence of DRX.

$$X_{DRX} = \frac{b}{a} = \frac{(\sigma_{WH} - \sigma)}{(\sigma_s - \sigma_{ss})} \quad (1)$$

Figures 5(a) to 5(c) show the θ vs σ plots for strain rates 0.1/s, 1.0/s, and 10.0/s, respectively, for different temperatures. These plots are used to estimate the stresses σ_s and σ_{ss}, as described in the section above.

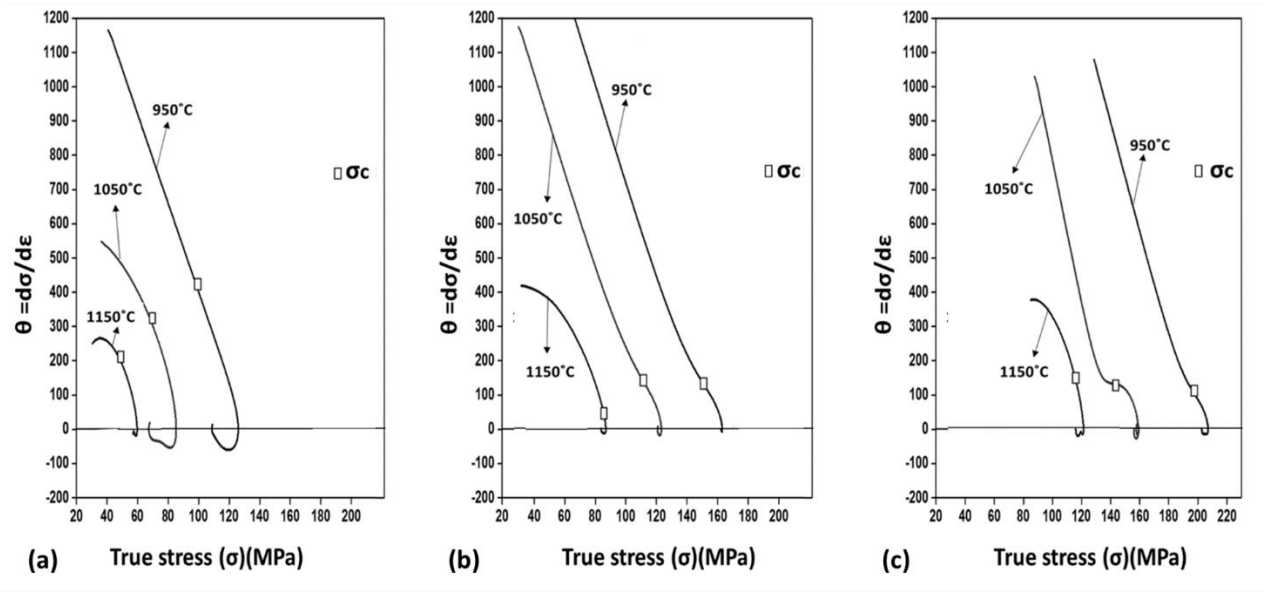

Figure 5: Variation of θ against σ plots at different temperatures for strain rates a) 0.1 /s, b) 1.0 /s and c) 10.0 /s.

Figure 6 shows the - (∂ θ /∂ σ) vs. σ plots for strain rates of 0.1, 1.0, and 10/s. These plots are used to estimate the values of critical flow stress for dynamic recrystallization (σ_c) that correspond to the stress values at the inflection point of - (∂ θ /∂ σ) vs. σ plots for different temperatures and strain rates.

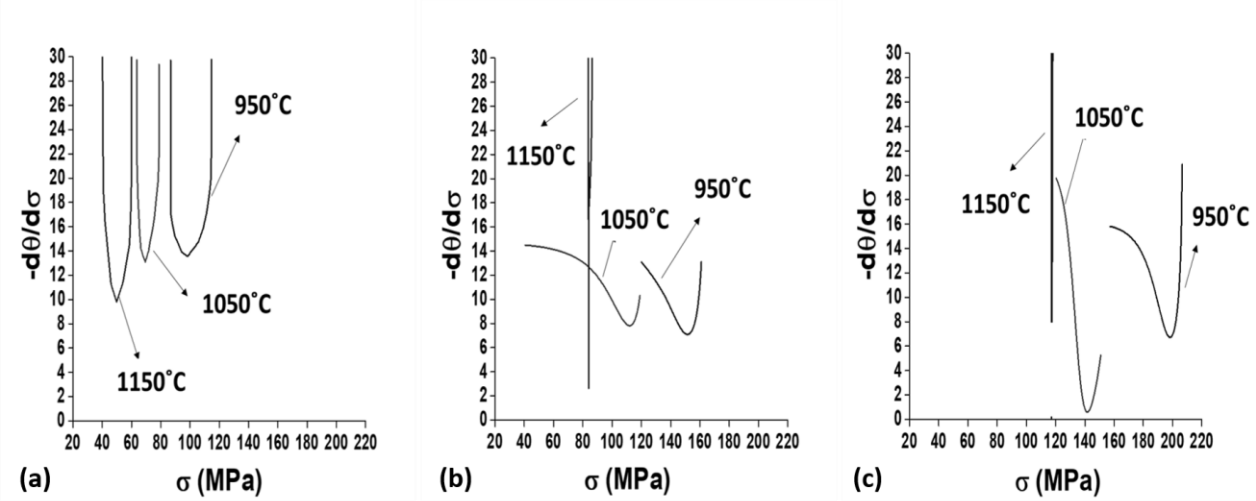

Figure 6: Variation of $-(d\theta/d\sigma)$ against σ at different temperatures for strain rates a) 0.1 /s, b) 1.0 /s and c) 10.0 /s

In the absence of real data, the work hardening curve without dynamic softening of material is approximated by two straight lines: i) the tangent at critical stress on the stress-strain curve, and ii) a horizontal line at $\sigma = \sigma_S$. A similar approach was reported elsewhere **(Ref 19)**. The value of σ_{WH} at different strain values are calculated using straight line approximations of the work hardening curve.

The calculated volume percentage of DRX values at different strain rates and temperatures for different true strain values are tabulated in Table 2. Table 2 shows that DRX percentages increase with a decrease in strain rates and an increase in temperature for all strains. Also, the DRX percentage increases with an increase in the extent of deformation (strain) for a particular strain rate and temperature. The literature also reported a similar observation (Ref 5, 14, 19). However, there are some discrepancies at higher strain due to the upward movement of the flow stress curve, as discussed above.

Table 2: Estimated volume fraction of dynamically recrystallized grains at different temperatures and strain rates at 70% deformation

Temperature (˚C) - strain rate (/s)	σ_c	σ_s	σ_{ss}	σ_{WH}	σ	X_{DRX}	σ_{WH}	σ	X_{DRX}	σ_{WH}	σ	X_{DRX}
	MPa	MPa	MPa	MPa	MPa	%	MPa	MPa	%	MPa	MPa	%
				0.4 true strain			**0.6 true strain**			**0.8 true strain**		
950-0.1	111	141	109	132	120	36	134	112	70	137	110	82
1050-0.1	70	102	69	93	767	47	95	70	75	98	69	88
1150-0.1	52	67	55	64	56	68	66	57	75	68	57	92
950-1.0	144	172	162	168	162	25	168	162	67	171	165	52
1050-1.0	107	136	123	127	123	33	130	121	69	129	124	70
1150-1.0	75	97	84	93	87	46	94	83	82	95	85	79
950-10.0	168	210	196	207	206	8	207	204	19	208	205	24
1050-10.0	144	165	157	160	159	19	162	159	31	163	158	64
1150-10.0	100	135	117	127	121	34	129	121	44	131	117	78

Fig.7 (a-d) shows the Inverse Pole Figure (IPF) maps of the deformed samples (obtained from electron backscattered diffraction analysis, EBSD) for different deformation temperatures and strain rates. In order to make the prior austenite grains more clearly visible, some optical micrographs etched with picric acid are made (**Ref 34**). Fig. 8(a-d) shows the picric acid-etched optical micrographs of the deformed sample at different temperatures and strain rates. At a lower temperature (950˚C), and strain rates (0.1/s), partial recrystallization is observed (Figs. 7 & 8(a)). Most of them are deformed non-recrystallized grains with few small recrystallized grains. At higher temperature (1150˚C) extent of recrystallization become significant (Figs. 7 & 8(b)). At a high strain rate (10/s), partially recrystallized prior austenite grains aligned along a certain direction. This could be a shear band providing sites for recrystallization (Figs. 7 & 8(d)). Although shear bands are observed at high strain rates and low temperatures (Figs. 7 & 8(c)), the fraction of recrystallized grains is much smaller, consistent with Table 2.

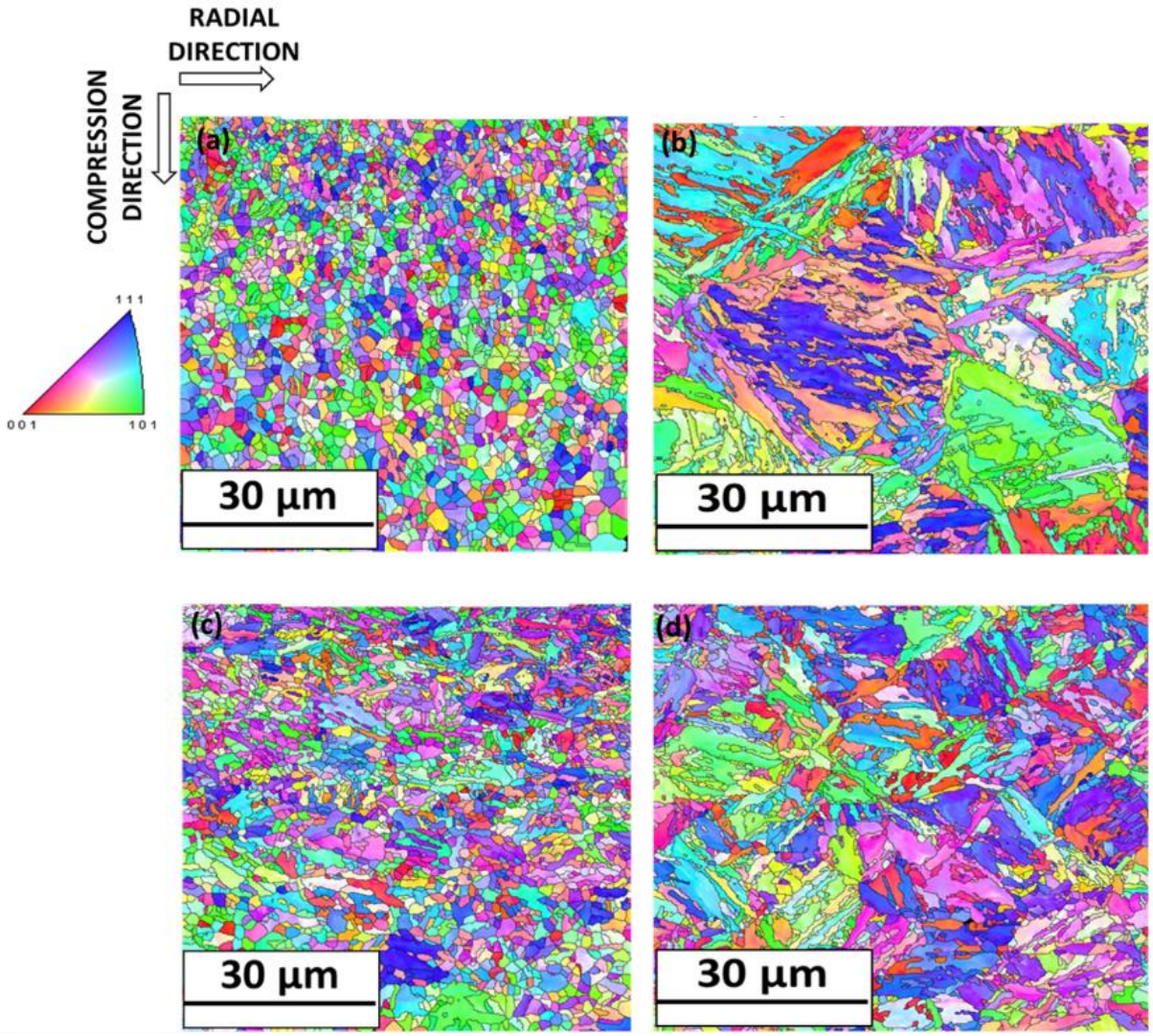

Figure 7: Inverse pole figure maps of various deformation conditions, a) 950-0.1-70, b) 1150-0.1-70, c) 950-10.0-70 and d) 1150-10.0-70. The compression direction is indicated. The colour legend for IPF orientation maps is also inserted.

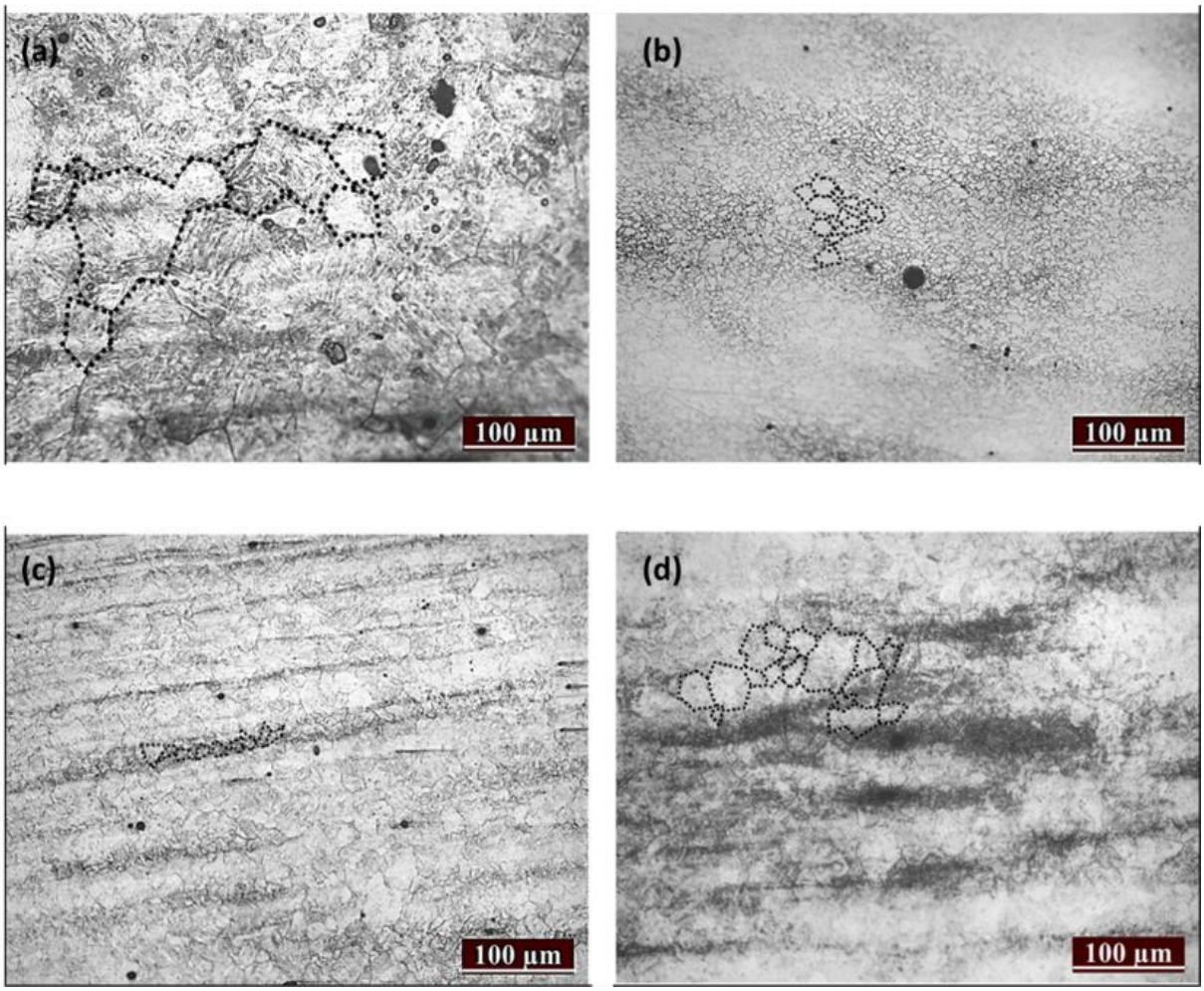

Figure 8: Optical micrographs of different deformation conditions a) 950-.1-70, b) 1150-0.1-70, c) 950-10.0-70 and d) 1150-10.0-70. Boundaries of some of the prior-austenite grains are delineated by black-dotted lines.

3.4. Processing Map

Processing maps provide guidelines to identify the range of operating parameters where hot deformation could be carried out safely without causing damage to the material. The Processing maps are generated by superimposing the contour maps of the two parameters. They are the efficiency of the power dissipation parameter (η) and the instability parameter (ξ) (Ref. 38). The power dissipation parameter (η) defines the fraction of energy used for microstructural evolution to the total energy consumed, including heat dissipation during plastic deformation. During hot deformation, the microstructural evolution can be favourable, i.e., a uniformly deformed structure comprising of fine and equiaxed DRX grains free from defects. The evolution of unfavourable microstructure might be due to extensive strain hardening, heterogeneous deformation and the associated deformation banding, and crack initiation and

propagation from the particles and inclusions. A high η value might represent a region where DRX occurs readily, as well as a region containing unfavourable microstructure that leads to the formation of cracks and voids. Therefore, to identify a safe deformation region, another parameter called the instability parameter, ξ, is introduced in the processing map. It represents an unstable region that encompasses only the negative values of ξ. It traces the strain rate and temperature limit where flow localization occurs and defects like voids and cracks generate under specific hot deformation conditions.

The flow stress, temperature, and strain rates are interdependent for a plastically deforming material. For constant strain and temperature, their inter-relationship is given by a power law (Equation 2), where the exponent is the strain rate sensitivity parameter.

$$\sigma = K\,\dot{\varepsilon}^{m} \tag{2}$$

The strain rate sensitivity (m) values, defined by equation (2), are obtained from the slopes at any strain rate on the fitted curve (2nd order polynomial) of ln (σ) vs. ln ($\dot{\varepsilon}$). The reliability of interpolation at intermediate strain rate values is well justified by considering a perfect polynomial fit with more than 95% goodness of fit in any case in the present study. It is to be noted that such 'm' values represent a condition of a particular strain and temperature.

$$m = \frac{\partial\left(ln(\sigma)\right)}{\partial\left(ln(\varepsilon)\right)} \tag{3}$$

The efficiency of the power dissipation parameter can be calculated from the strain rate sensitivity parameter (m) by equation (4), following **(Ref 38).**

$$\eta = \frac{2m}{(m+1)} \tag{4}$$

The instability parameter ξ ($\dot{\boldsymbol{\varepsilon}}$), which helps to delineate regions where unstable flow, fracture, or defect are likely to occur, can be estimated by equation (5), following **(Ref 38).**

$$\zeta(\dot{\varepsilon}) = \frac{\partial ln\left(\frac{m}{m+1}\right)}{\partial ln(\dot{\varepsilon})} + m \tag{5}$$

It is calculated from the values of slopes at any strain rate on the fitted polynomial curve of $ln\left(\frac{m}{m+1}\right)$ Vs. $ln(\dot{\varepsilon})$.

Figure 9 shows the processing maps at various true strain values. These maps superimposed the efficiency of power dissipation (η) and instability (ξ) contours. The hatched area represents the instability region containing only the negative values of ξ, where microstructural energy dissipation is likely to produce defects like cracks. It may be noted that the contours shown in the unstable hatched region depict the η contours only. A dotted square box indicates the safe zone of deformation outside the instability region and energy dissipation efficiency greater than 30% (Ref 4, 20). Even outside the instability zone, the low energy efficiency region (below 30%) is not included in the safe region.

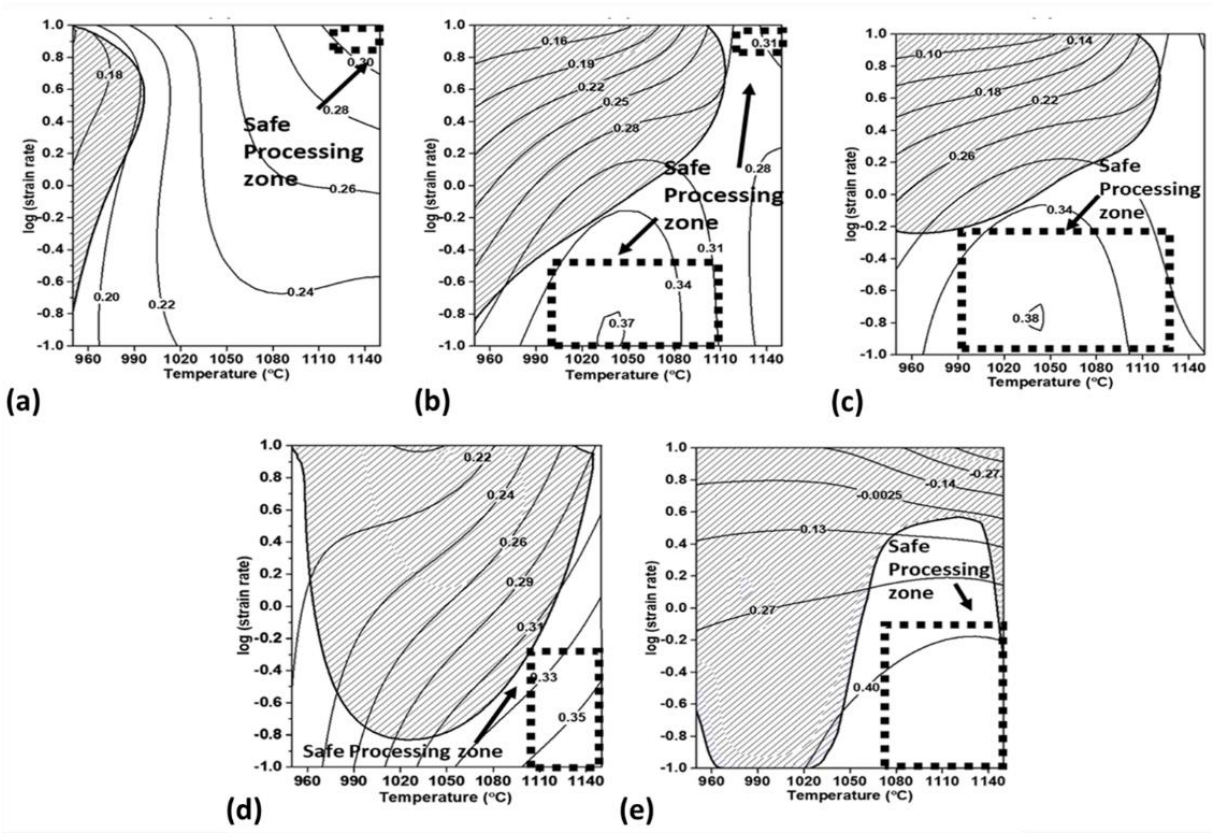

Figure 9: Processing maps of EN30B steel at true stains a) 0.4, b) 0.6, c) 0.8, d) 1.0, and (e) 1.2. The lines with numbers indicate the η contours, and the hatched area indicate the instability region with only negative values of ξ. The dotted boxes indicate the safe zone of deformation with efficiency of power dissipation greater than 30%.

At low strain (0.4), the safe deformation zone is limited to a very narrow window in the right top corner (high strain rates in the range of 6 to 10/s and high temperatures in the range 1110-

1150˚C). However, the instability region remains restricted on the left face at lower temperatures (<990˚C). Thus, most white regions are unsuitable for safe deformation outside the instability zone.

At a higher strain of 0.6, the instability zone expands from left to right, encompassing a large temperature regime, especially for higher strain rates. The safe zone moves to the middle bottom encompassing temperatures in the range of 1010 to 1110˚C and lower strain rates in the range of 0.1 to 0.3/s. Also, a small region at the right top corner also exists as a safe zone, similar to the low strain at 0.4. With a further increase in strain to 0.8, the instability region moves up, clearing the entire low strain regime irrespective of temperature. The safe deformation region expands at the middle bottom, with wider temperatures (990-1130˚C) and strain rates (0.1-0.6/s). At a strain of 1.0, the instability region expands significantly and dips down, while the safe zone is pushed further to the right bottom corner, encompassing high temperatures (1100-1140˚C) at low strain rates (0.1 to 0.5 /s). With a further increase in strain to 1.2, the safe deformation zone remains at the right bottom corner but expands to broader temperatures (1070-1150˚C) and strain rates (0.1 to 0.8/s). Such shifting of the safe deformation zone with strain was also reported in the literature **(Ref. 4).**

The evolution of a safe deformation zone with strain may be explained as follows. Low strain rates and higher temperatures promote the growth of dynamically recrystallized (DRX) grain in the strained matrix. DRX also increases with strains due to the generation of defects (like dislocations, twins, and deformation bands), which act as the nucleation sites for recrystallized grains. At low strain, defect generation in the matrix is less, which minimizes the nucleation of new strain-free grains. In the absence of recrystallization, work hardening dominates, making the matrix more resistant to further deformation, corresponding to a low energy dissipation efficiency value. However, a safe zone in a small top-right window (high strain rates and temperatures) may be explained as follows. At high strain rates, time to deformation is limited for any strain level. Hence, dislocations generate rapidly, and those get less time to annihilate or rearrange. As a result, high dislocation density can increase the local strain energy, i.e., the driving force for dynamic recrystallization. Moreover, high temperature increases dislocation mobility through the thermally activated atomic migration, facilitating dislocation motion by climb and cross-slip mechanisms. Thus, at low strains, favourable microstructural change with high efficiency of energy dissipation is likely to be observed at high strain rates and high-temperature regimes.

At higher strain levels, the prevailing high density of defects (dislocations, twins, deformation bands, etc.) increases the driving force for recrystallization. These defects offer sites for the nucleation of recrystallized grains. At that condition, recrystallization is promoted at lower strain rates and higher temperatures that allows more atomic diffusion. Therefore, at strains 0.6 and above, the safe zone moves to low strain rates and high temperatures where dynamic recrystallization is promoted (Table-2). However, the instability zones also expand at higher strains, pushing the safe zone further to higher temperatures. In fact, there is a competition between favourable and unfavourable microstructural evolution at higher strains. For example, when heavy deformation is applied at a higher temperature, adiabatic deformation heating may cause inhomogeneous strain distribution by the formation of the adiabatic shear band. When those bands become severe, cracks can form along those bands, expanding the instability region. When those bands are mild, such shear bands may act as the nucleation sites for new dynamically recrystallized grains (decreasing instability region). Fig. 8(d) may be referred to show such recrystallized grain along with the shear band. Therefore, the safe zone is found to widen for a transition of strain from 1.0 to 1.2, which may be attributed to shear bands allowing some growth of DRX grains, reducing the instability region.

3.5.Inclusion evolution

Figure 10 depicts the SEM images of all the thermo-mechanically treated unetched samples at all temperatures and strain rates at 70% deformation. The images of inclusions at 950˚C and 0.1 strain rate (4 boxes in the lower left corner) show the de-bonded inclusions with the matrix. Cavities were seen, with no cracks identified. Cracks appear in images at higher strain rates of 1.0/s (four middle bottom boxes) and 10.0/s (four right bottom boxes). No prominent cracks are observed at higher temperatures (1050 and 1150˚C) except at 1150˚C and high strain rate (10/s), as depicted in the top right four boxes.

The effect of inclusions on deformation behaviour is discussed below. Figure 10 depicts no cracks at lower strain rates (0.1/sec). However, de-bonding develops between the inclusions and steel matrix, leading to micro-voids generation. Nevertheless, such micro-voids could not propagate forming a higher volume fraction of softer recrystallized grains at the low strain rate of 0.1/sec (see Table 2). However, at higher strain rates, the volume fraction of recrystallized grains decreases, and these voids increases in size from 1-2 μm to 2-7 μm with increasing strain rates above 1/s and at lower temperatures (<1050˚C). Coalescence and converging of these

voids occur near the inclusion forming an unstable region designated by negative values of ξ (see Figure 9) at higher strain rates and lower temperatures.

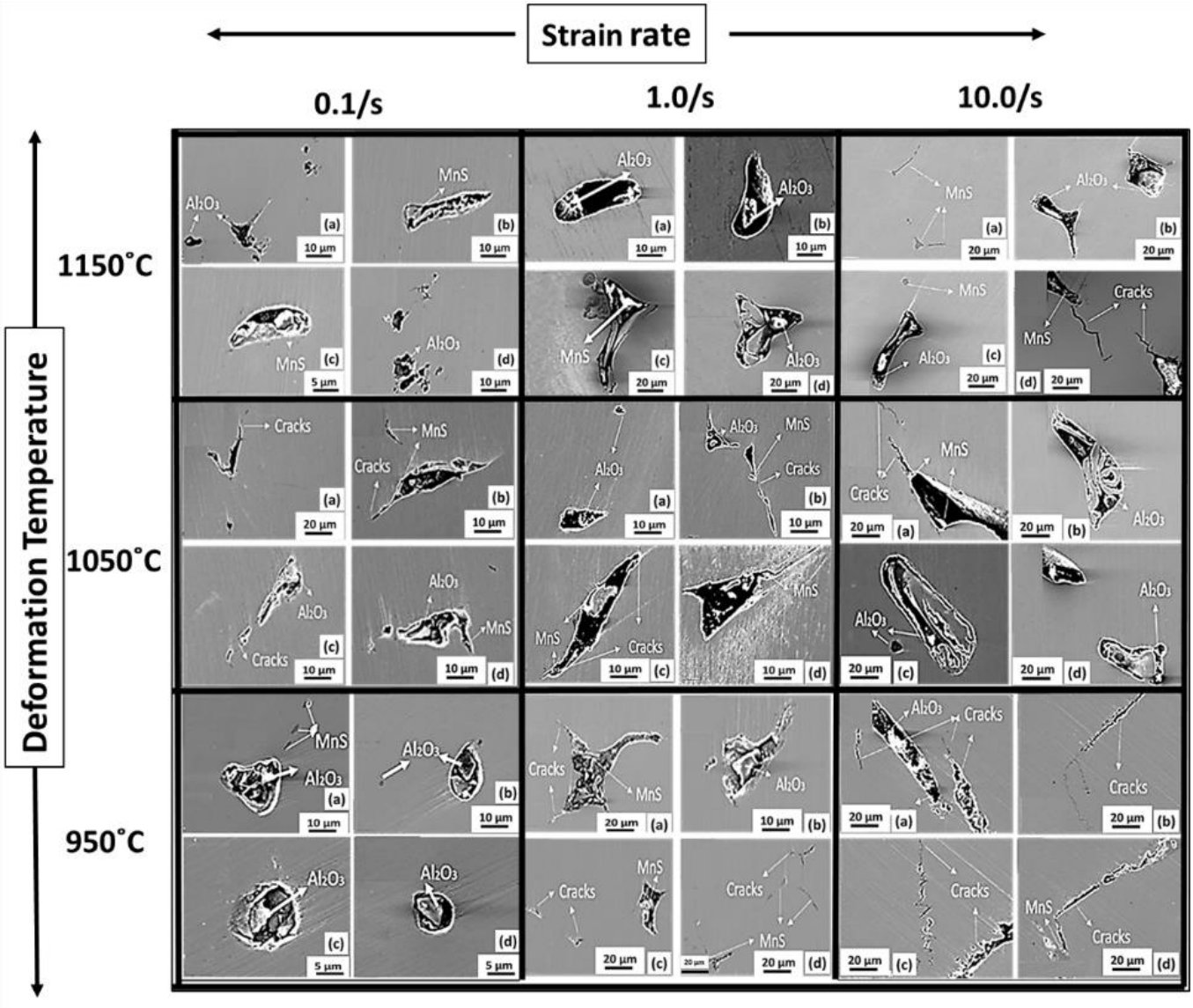

Figure 10: a) SEM images at different deformation temperatures and strain rates from four different locations.

In this context, it is necessary to understand the combined effect of straining and DRX of the ferrite matrix and defect generation during hot deformation in the presence of inclusions. Dislocation loops form around the inclusions by virtue of stress and strain concentration around inclusions and dislocation-inclusion interaction. The number of dislocation loops increases with the increase in applied stress. The loops adjacent to the inclusions are pushed into the inclusion-matrix interface by the repulsive force of the surrounding loops. Thus, voids are initiated by separating the inclusion-matrix interface for weakly bonded inclusions having a

significant difference in elastic and thermal properties with the matrix (**Ref 37)**. When the applied external stress exceeds the nucleation threshold stress for void formation, cavities form in the material. Subsequently, the voids grow by further dislocation activities aided by the triaxial stress field acting around the voids.

The DRX of the matrix releases the strain concentration, i.e., significantly reduces the dislocation density around the inclusions. As a result, void nucleation can be restricted, and a higher strain can be required to initiate the voids. The DRX phenomenon also relieves the strain in the matrix ligament between the two adjacent voids. As a consequence, void coalescence is also delayed. Overall, the deformability of the steel is enhanced. Under high-temperature deformation (900˚C–1200˚C), stress strengthening caused by the inclusions and stress softening caused by DRX determine the overall strength, while the promotion of void initiation and growth by inclusions and the inhibition of void growth and coalescence by DRX jointly determine the plasticity **(Ref 39-40)**.

At lower deformation temperatures, the preferential deformation of the matrix surrounding hard inclusions can result in the formation of shear bands that leads to deformation instability **(Ref 41).** As the instability region shrinks at the higher temperature (Figure 9), the propensity of crack formation also decreases. By examining the middle row boxes (figure 10) representing 1050˚C, few cracks could be found at the highest strain rates at 10/sec. The propensity for crack formation decreases at higher temperature, 1150˚C.

A decrease in MnS in the matrix was observed at all deformation temperatures, especially at 1150˚C. It was observed that before the thermo-mechanical treatment, the size of inclusions was in the range of 10-40 µm. After the treatment, the size was reduced with increasing deformation temperature, ranging between 5-10 µm, indicating the dissolution of MnS. Besides, the volume fraction of dynamically recrystallized grains also increased at higher temperatures (see Table 2). Therefore, crack formation is limited at high temperatures, even at high strain rates.

It may be observed from Figure 10 that MnS inclusions get deformed, elongated, and alumina inclusions are fragmented, as reported by previous investigators **(Ref 5, 24, 27).** While MnS are plastic and absorb energy by deforming, alumina inclusion is harder and cannot absorb energy. Instead, they lead to stress concentration at the matrix-inclusion interface. On the other hand, as plastic inclusions get deformed, the stress field along the weak bonded inclusion and matrix expands. When such stress field from adjacent inclusions overlaps, causing a fault in conjunction with two adjacent plastic inclusions **(Ref 24)**. As per recent studies, the

deformability of plastic inclusion, softer than the matrix, increases with the increase in the difference in hardness and viscosity between the matrix and inclusion **(Ref 37, 42)**. In complex inclusions, embedding both Al_2O_3 and MnS might be more dangerous because the mutual interaction of strain fields around these inclusions is likely to amplify the strain and initiate cracks. Besides, the overall size of compound inclusions is larger than the individual inclusions. From Figure 10, it is also observed that cracks are generated at complex inclusions where both Al_2O_3 and MnS are embedded. Through a mathematical model, it is demonstrated that compound inclusion assists crack formation more easily than individual inclusions **(Ref 43).**

4. Conclusion

Three safe deformation zones for hot deformation of EN30B steel are identified at low, medium, and high strain levels. At low strain (true strain 0.4), the safe deformation zone locates at high temperatures (1110-1150˚C) and high strain rates (6 to 10 s^{-1}) regime. At medium strain (0.6 to 0.8), the safe zone shifts to a low strain rate (0.1 to 0.6 s^{-1}) and wide temperatures (990 to 1130˚C) regime. At high strains (1.0 to 1.2), the safe zone shifts to a higher temperature (1070-1150˚C) but with broader strain rates range of 0.1 to 0.8 s^{-1}. At higher strains, shear bands in the deformed body might assist in dynamic recrystallization or generate fault depending on the local strain values. Estimated recrystallized grains were found to be maximum at low strains and high temperatures delineating the safe zone. Cracks were found to originate at complex inclusions at lower temperatures and higher strain rates, which are encompassed by the instability regime in the processing map, irrespective of strain values.

The present study proposes an optimized schedule for forging rather than a fixed deformation condition. Usually, industrial forging is a multi-pass process. Therefore we can recommend a high strain rate during initial passes and then low strain rates for subsequent passes. We also recommend that the temperature of forging should be progressively increased for subsequent passes. Future studies may involve testing such schedules on an industrial scale. On fundamental study, a more detailed evolution of inclusions in terms of counts, size, shape, and composition and its correlation with the processing map would further clarify the defect generation during hot deformation of EN30B steel in the presence of inclusion.

5. Acknowledgement

The work is funded by the Department of Heavy Industries (DHI), New Delhi, Govt. of India and Heavy Engineering Corporation Limited (HEC), Ranchi, India.

6. Conflict of Interest

On behalf of all authors, the corresponding author states that there is no conflict of interest.

7. References

[1] C. Wu, and S. Han, Mechanical and microstructure properties of the Ni-Cr-Mo modified steel by heat treatment process, IOP Conf. Ser.: Mater. Sci. Eng., 2018, 359, p 012027 (1-7).

[2] Y.C. Lin, M.S. Chen, and J. Zhong, Numerical simulation for stress/strain distribution and microstructural evolution in 42CrMo steel during hot upsetting process, Computational Materials Science., 2008, 43(4), p 1117–1122.

[3] Y.C. Lin, M. S. Chen, and J Zhong, Constitutive modelling for elevated temperature flow behaviour of 42CrMo steel, Computational Materials Science 42, 2008, 470-477.

[4] K.Chadha, D.Shahriari, and M.Jahazi, Constitutive modelling of ingot breakdown process of low alloy steels, La Metallurgia Italiana Modellazione, 2016, 4, p 5-12.

[5] Y.C. Lin, and G. Liu, Effects of strain on the workability of a high strength low alloy steel in hot compression, Materials Science and Engineering A., 2009, 523, p 139–144.

[6] M.S. Chen, Y.C. Lin, and X.S. Ma, The kinetics of dynamic recrystallization of 42CrMo steel, Materials Science and Engineering A., 2012, 556, p 260-266.

[7] G.Z. Quan, Y. Wang, Y.Y. Liu, and J. Zhou, Effect of Temperatures and Strain Rates on the Average Size of Grains Refined by Dynamic Recrystallization for as-extruded 42CrMo Steel, Materials Research, 2013, 16(5), p 1092-1105.

[8] S. V. Sajadi Far, M. Ketabchi, and M.R. Nourani, Hot Deformation Characteristics of 34CrMo4 Steel, journal of iron and steel research, international, 2010, 17(12), p 65-69.

[9] S. V. Sajadifar, M. Ketabchi, and M. Nourani, mathematical modeling for 34CrMo4 steel during hot compression, Metall. Mater. Eng., 2012, 18 (1), p. 9-17.

[10] Z. Xiao, Y. Huang, and Y. Liu, Plastic deformation behaviour and Processing Maps of 35CrMo steel, Journal of Materials Engineering and Performance, 2016, 25, p. 1219-1227.

[11] M. I. Mehta, B.P. Kashyap, and R. K. P.Singh, Study on Flow Properties of Rotor Grade Steel, 2016, Journal of Metallurgy and Materials Science, Vol. 58, No. 4,, p. 221-229.
[12] A. Momeni, S.M. Abbasi, and H. Badri, Hot deformation behavior and constitutive modeling of VCN200 low alloy steel, Applied Mathematical Modelling, 2012, 36, p 5624–5632.
[13] M. Mirzaee, H. Keshmiri, G. R Ebrahimi, and A. Momeni, Dynamic recrystallization and precipitation in low carbon low alloy steel 26NiCrMoV 14-5, Materials Science and Engineering A, 2012, 551, p 25– 31.

[14] M. R. G. Ferdowsi, D. Nakhaie, P. H. Benhangi, and G. R. Ebrahimi, Modeling the High Temperature Flow Behavior and Dynamic Recrystallization Kinetics of a Medium Carbon Microalloyed Steel, JMEPEG, 2014, 23, p 1077–1087.
[15] F. Zhang, Y. Yang, Q. Shan, Z. Li, J. Bi, and R. Zhou, Microstructure Evolution and Mechanical Properties of 0.4C-Si-Mn-Cr Steel during High Temperature Deformation, 2020, Materials, 13, 172, p 1-11.
[16] G-L. Wu, Y-J. Zhang, and S-W. Wu, Characterization of hot deformation behaviour of Nb-Ti microalloyed high strength steel, The Journal of the Southern African Institute of Mining and Metallurgy, 2019, 119, p 503-508.
[17] M. Sadeghi, M. Hadi, O. Bayat and H. Karimi, Hot Deformation of the Mn-Ni-Cr Alloy During Compression, Iranian Journal of Materials Science & Engineering, 2020, 17, No. 1, p 102-108.

[18] S. V. Sajadifar, M. Ketabchi, and B. Bemanizadeh, dynamic recrystallization behavior and hot deformation characteristics in 4340 steel, Metallurgist, 2012, Vol. 56, Nos. 3–4, p 310-320.

[19] X. Yang, H. Guo, Z. Yao, and S. Yuan, Flow Behaviour and Dynamic Recrystallization of BT25y Titanium Alloy During Hot Deformation, High Temp. Mater. Process., 2018, 37(2), p 181–192.

[20] S. Jian, L. Jinghui, P. Wang, and Z. Huang, Hot Deformation Behaviour, Dynamic Recrystallization and Processing Map of Fe–30Mn–10Al–1C Low-Density Steel. Trans. Indian Inst. Met., 2021, 75, p 699–716.
[21] Y.C. Lin, X Y Wua, X. M. Chen, J. Chen, D. X. Wena, J L Zhang, and L.T Li, EBSD study of a hot deformed nickel-based superalloy, Journal of Alloys and Compounds, 2015, 640, p 101–113.

[22] M. S. Chen, Y.C. Lin, and K.K. Li, Dynamic recrystallization behaviors of typical solution-treated and aged Ni- Based superalloy under steeped strain rates, Procedia Engineering, 2017, 207, p 2125–2130.

[23] Z. Chen, Y.C. Lin, D. G. H, Y. M. Lou, and M S Chen, A unified dislocation density-based model for an aged polycrystalline Ni-based superalloy considering the coupled effects of complicate deformation mechanisms and initial δ phase, Materials Science & Engineering A, 2021, 827, 142062.

[24] W.L. Zhao, Q.X. Ma, and S.L. Zha, Mechanism for Development of Faults Originating from Compound Inclusions in the Forging Process of 30Cr2Ni4MoV Heavy Ingots, Materials Transactions., 2014, 55(8), p 1324–1331.

[25] Z. Xiao, Y. Huang, H. Liu, and S. Wang, Hot Tensile and Fracture Behavior of 35CrMo Steel at Elevated Temperature and Strain Rate, Metals, 2016, 6, 210, p 1-11.

[26] N.K. Kanoje, S.C. Sharma, and S.P. Harsha, Subsurface crack propagation with different inclusions under a wheel flat LEFM Analysis. Int. J. Vehicle Noise and Vibration., 2015, 11(1), p 1–17.

[27] R.S. Qi, M. Jin, X. G. Liu, and B.F. Guo, Formation Mechanism of Inclusion Defects in Large Forged Pieces. J. Iron & Steel Res. Int., 2016, 23(6), p 531–538.

[28] V. Singh, R. Khan, B. Bandi, G.G. Roy, and P. Srirangam, Effect of non-metallic inclusions (NMI) on crack formation in forged steel, Materials Today: Proceedings, 2021, 41, 1096-1102.

[29] Y. Huo, B. Wang, J. Lin, Q. Bai, J. Hongchao, and T. Xuefeng, Hot compression deformation behaviour and microstructure evolution rule of a high-speed railway axle steel, Indian J. Eng. & Mater. Sci., 2017, 24(6), p 447–454.

[30] Andrews, K.W, Empirical formulae for the calculation of some transformation temperatures, J. Iron Steel Inst., 1965, 203(7), p 721-727.

[31] C. Ouchi, T. Sampei, and I. Kozasu, The Effect of Hot Rolling Condition and Chemical Composition on the Onset Temperature of γ-α Transformation after Hot Rolling, Trans. Iron and Steel Inst. Japan., 1982, 22(3), p 214-222.

[32] F. Boratto, R. Barbosa, S. Yue, and J. J. Jonas, Proc. of the 1st Conf. on Physical Metallurgy of Thermomechanical Processing of Steels and Other Metals (THERMEC-88), ISIJ. Tokyo, 1, 1988, p 383–390.

[33] F. Yin, L. Hua, H. Mao, X. Han, D. Qian, and R. Zhang, Microstructural modeling and simulation for GCr15 steel during elevated temperature deformation Mater. Des., 2014, 55, p 560–573.
[34] A. Chatterjee, D. Chakrabarti, A. Moitra, R. Mitra and A.K. Bhaduri, Effect of deformation temperature on the ductile–brittle transition behavior of a modified 9Cr–1Mo steel, Materials Science and Engineering A, 2015, 630, p. 58-70.
[35] Dieter, and E. George, Mechanical Metallurgy, SI Metric ed., McGraw-Hill Book Co., London, 1988, p 520-521.
[36] E. I. Poliak, and J. J. Jonass, A one-parameter approach to determining the critical conditions for the initiation of dynamic recrystallization, Acta Mater.,1996, 44(1) p 127–136.
[37] W. Yang, K. Peng, L. Zhang, and Q. Ren, Deformation and fracture of non-metallic inclusions in steel at different temperatures J. Mater. Res. Technol., 2020, 9(6), p 15016–15022.
[38] Prasad. Y. V. R. K, Rao. K. P, Sasidhara. S, Hot Working Guide, 2nd edition, ASM International, Ohio. USA. 2015, p 6-12.
[39] Xiaoqing Shang, Cui. Zhenshan, and M.W. Fu, Dynamic recrystallization based ductile fracture modeling in hot working of metallic materials, Int. J. Plast., 2017, 95, p 105–122.
[40] C. Wang, X. Liu, J. Gui, Z. Du, Z. Xu, and B. F. Guo, Effect of MnS inclusions on plastic deformation and fracture behavior of the steel matrix at high temperature, Vacuum., 2020, 174, p 109209 (1-11).
[41] M. Goudarzi, F. Corso, D. Bigoni, and A. Simone, Dispersion of rigid line inclusions as stiffeners and shear band instability triggers, Int. J. Solids Struct., 2021, 210, p 255–272.
[42] Y. Wang, L. Zhang, Y. Ren, L. Zushu, and C. Slater, Effect of compression temperature on deformation of CaO–CaS–Al2O3–MgO inclusions in pipeline steel, J. Mater. Res. Technol., 2021, 11, p 1220–1231.
[43] Z. Xianyan, S. Zhutao, T. Famin, H. Christopher, and Jiang. Jun, Microstructural effects on central crack formation in hot cross-wedge-rolled high-strength steel parts, J. of Mater. Sci., 2020, 55(22), p 9608-9622.

FIGURE 1

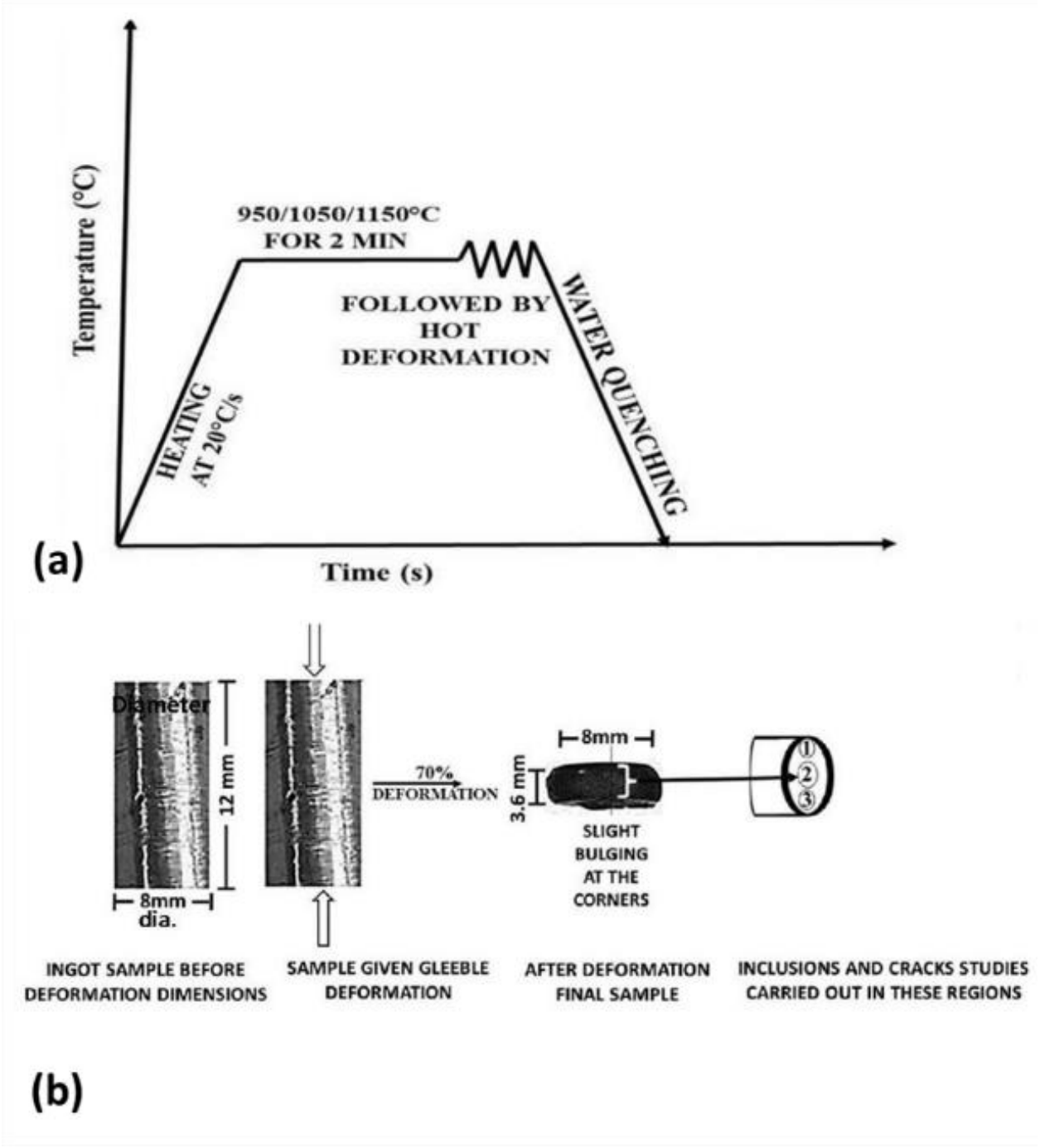
Temperature (°C)
950/1050/1150°C
FOR 2 MIN
FOLLOWED BY
HOT
DEFORMATION
WATER QUENCHING
HEATING
AT 20°C/s
Time (s)
(a)
Diameter
12 mm
8mm
dia.
70%
DEFORMATION
8mm
3.6 mm
SLIGHT
BULGING
AT THE
CORNERS
INGOT SAMPLE BEFORE
DEFORMATION DIMENSIONS
SAMPLE GIVEN GLEEBLE
DEFORMATION
AFTER DEFORMATION
FINAL SAMPLE
INCLUSIONS AND CRACKS STUDIES
CARRIED OUT IN THESE REGIONS
(b)

FIGURE 2

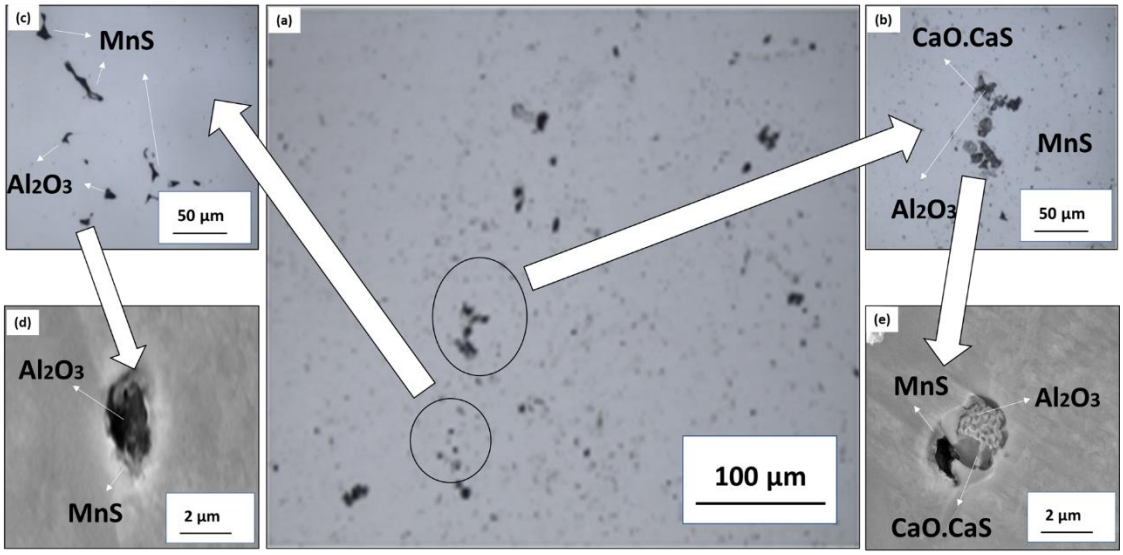
(c)
MnS
Al2O3
50 µm
(a)
100 µm
(b)
CaO.CaS
MnS
Al2O3
50 µm
(d)
Al2O3
MnS
2 µm
(e)
MnS
Al2O3
CaO.CaS
2 µm

FIGURE 3

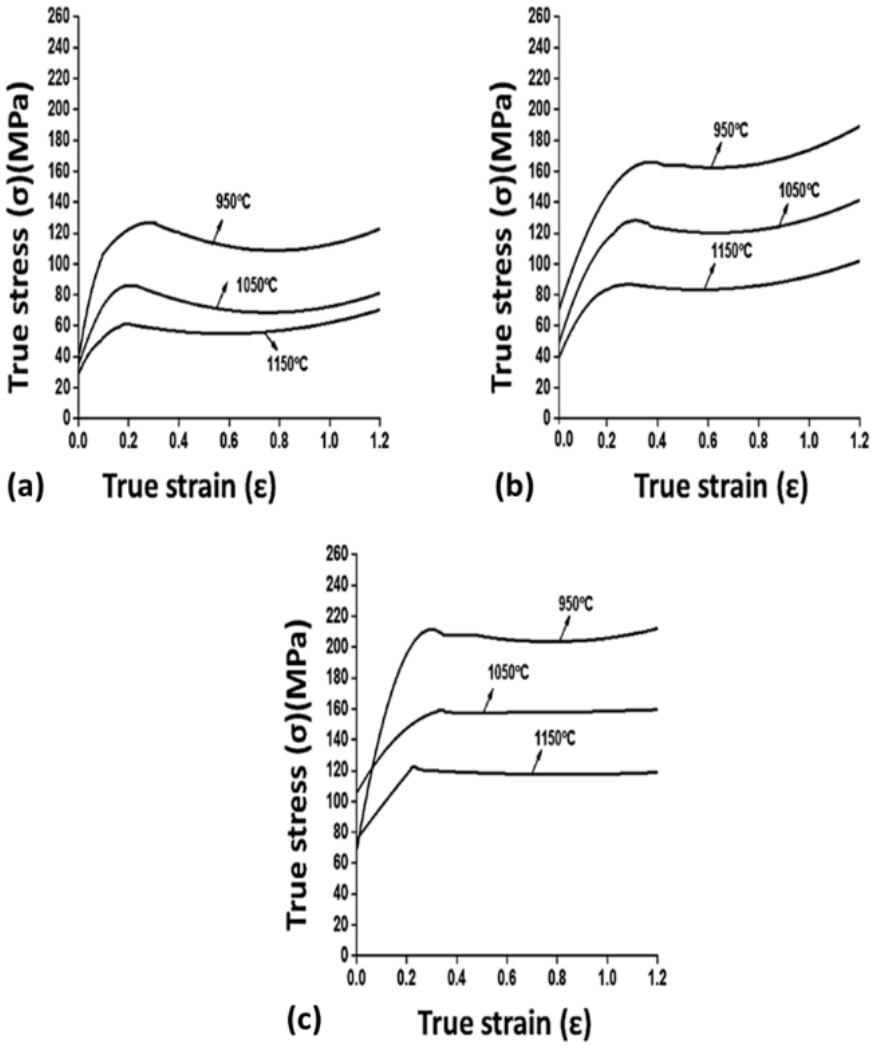

FIGURE 4

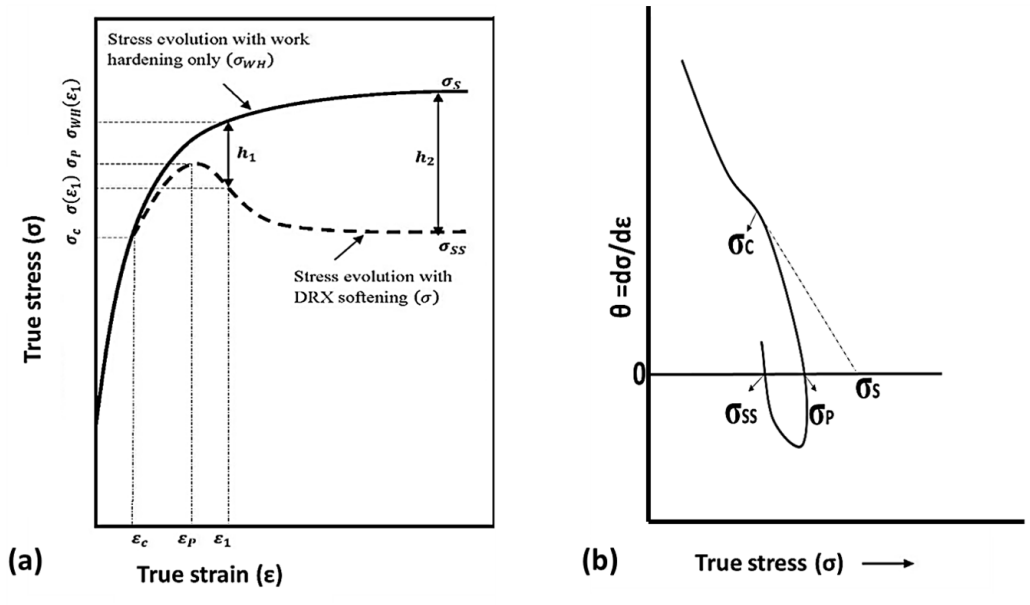

FIGURE 5

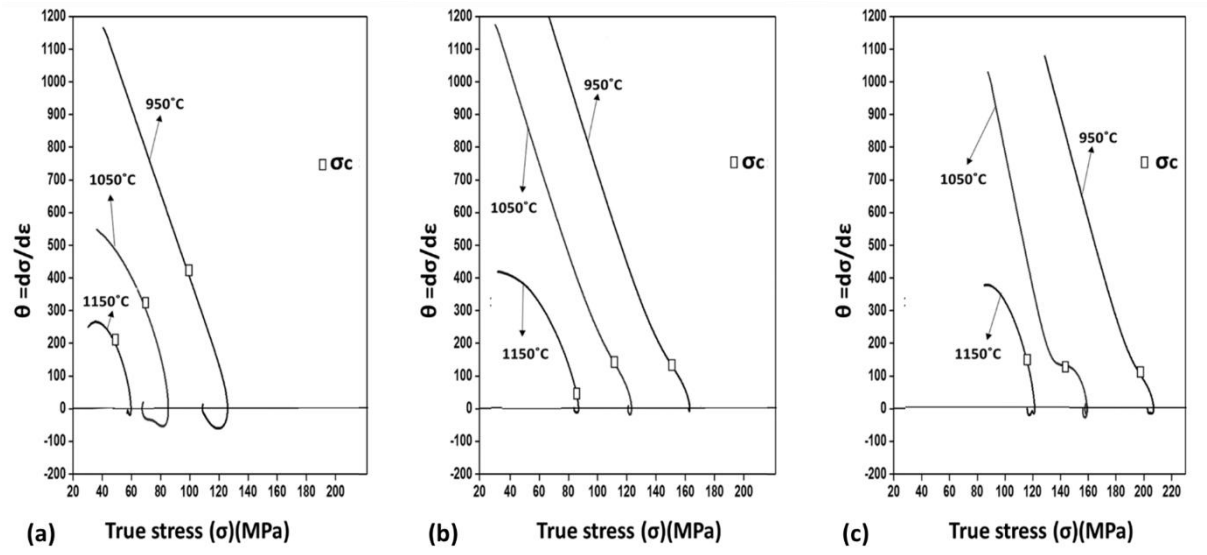

FIGURE 6

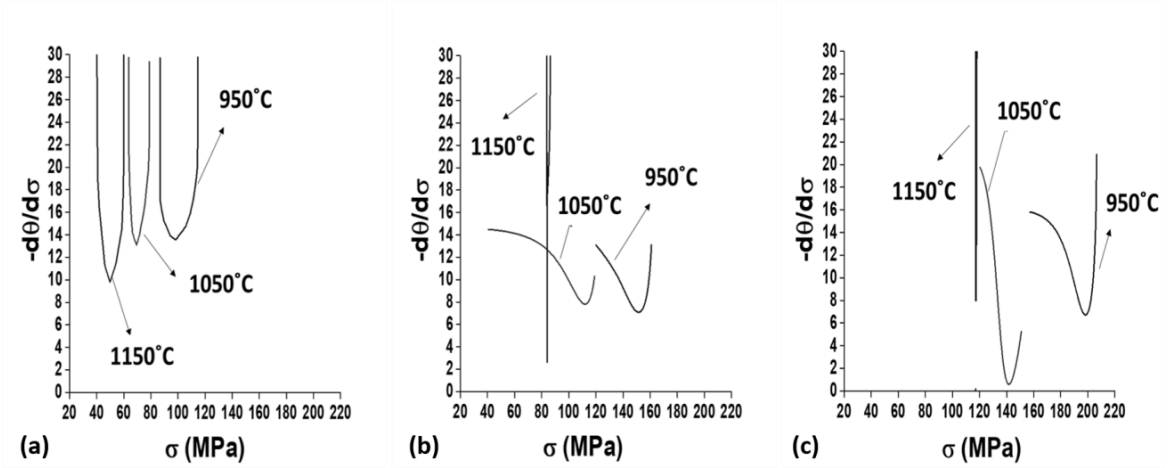

FIGURE 7

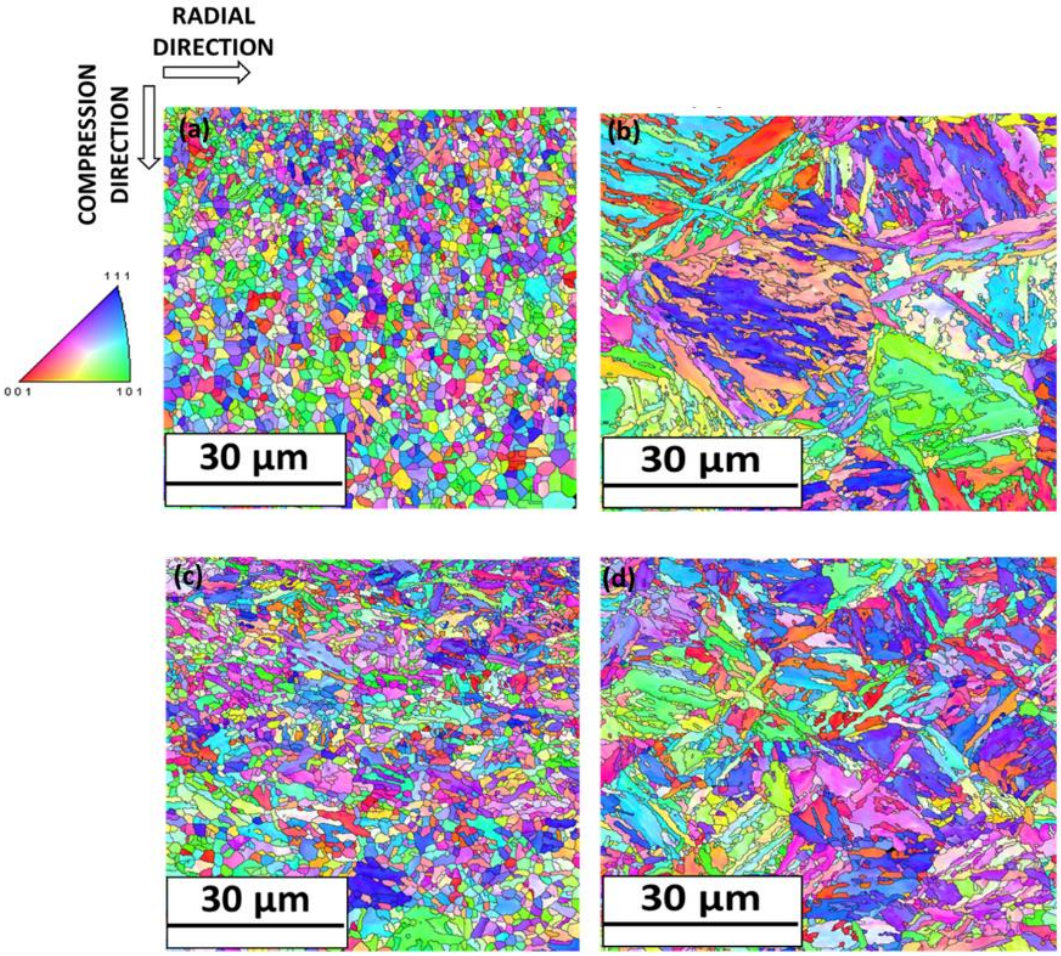

FIGURE 8

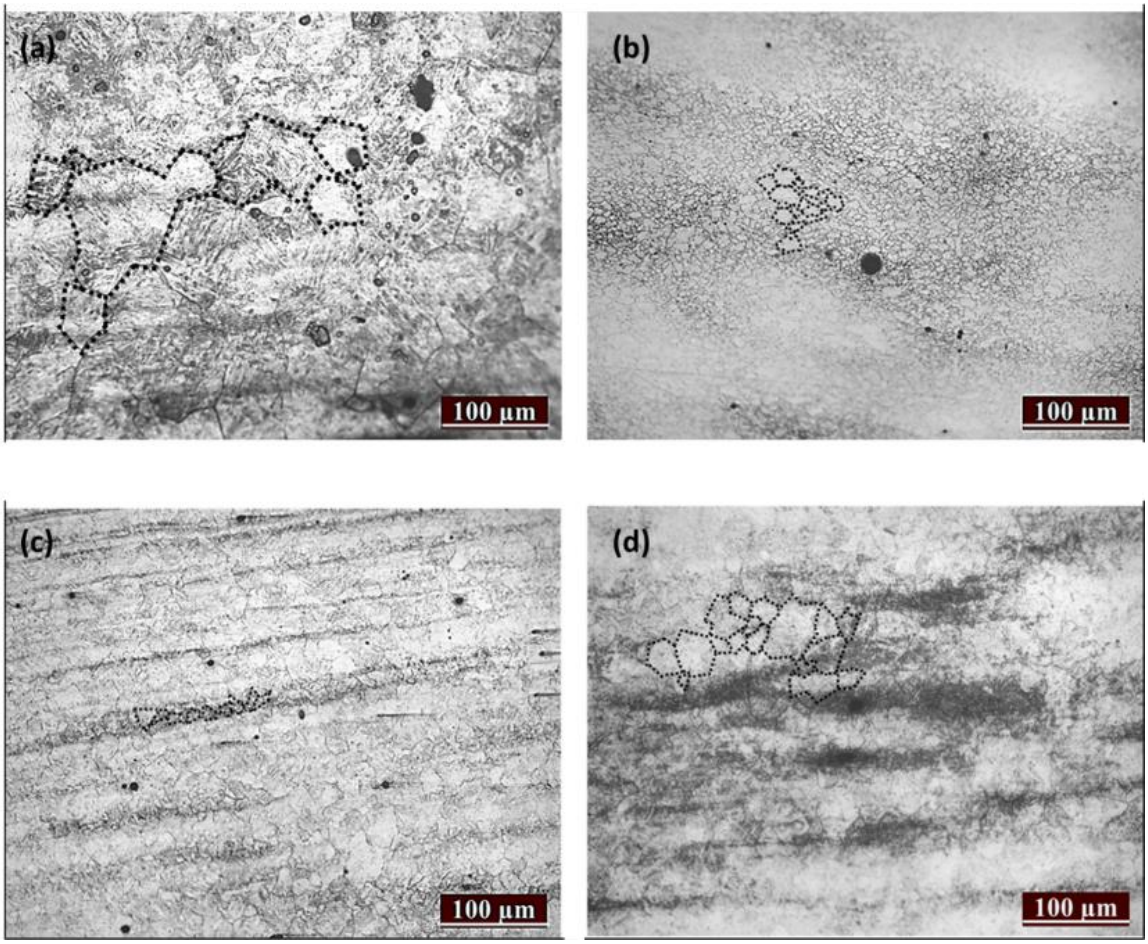

FIGURE 9

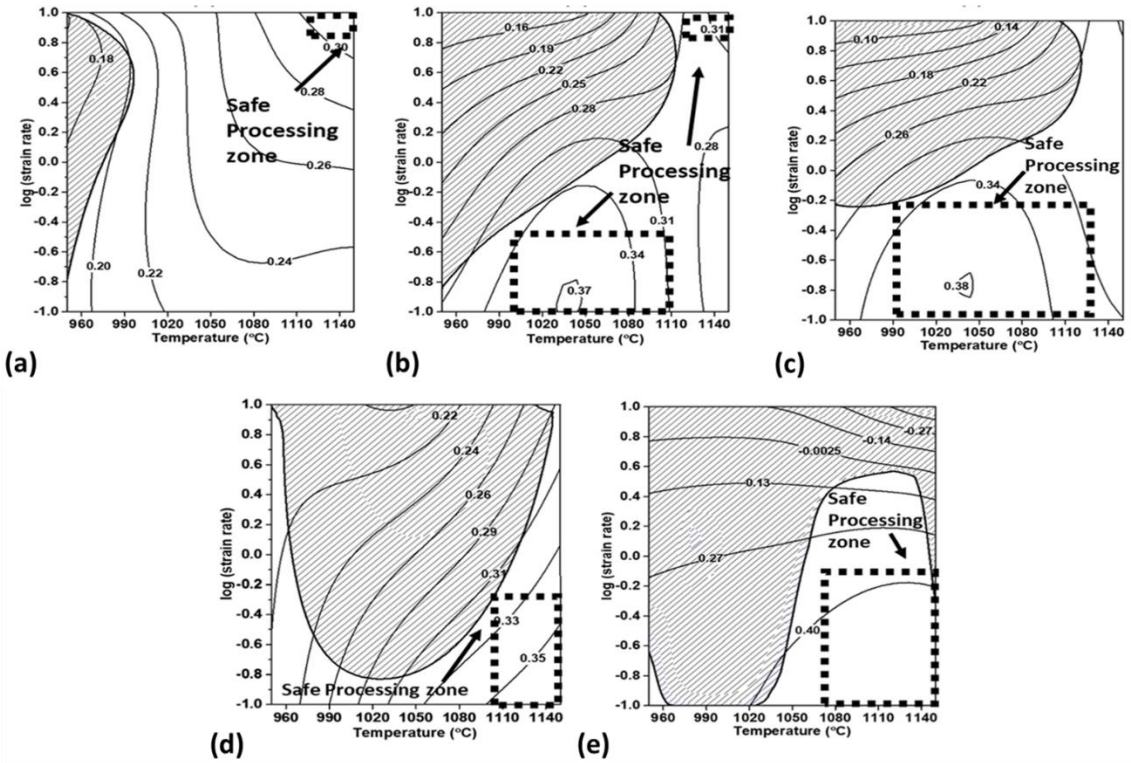

FIGURE 10

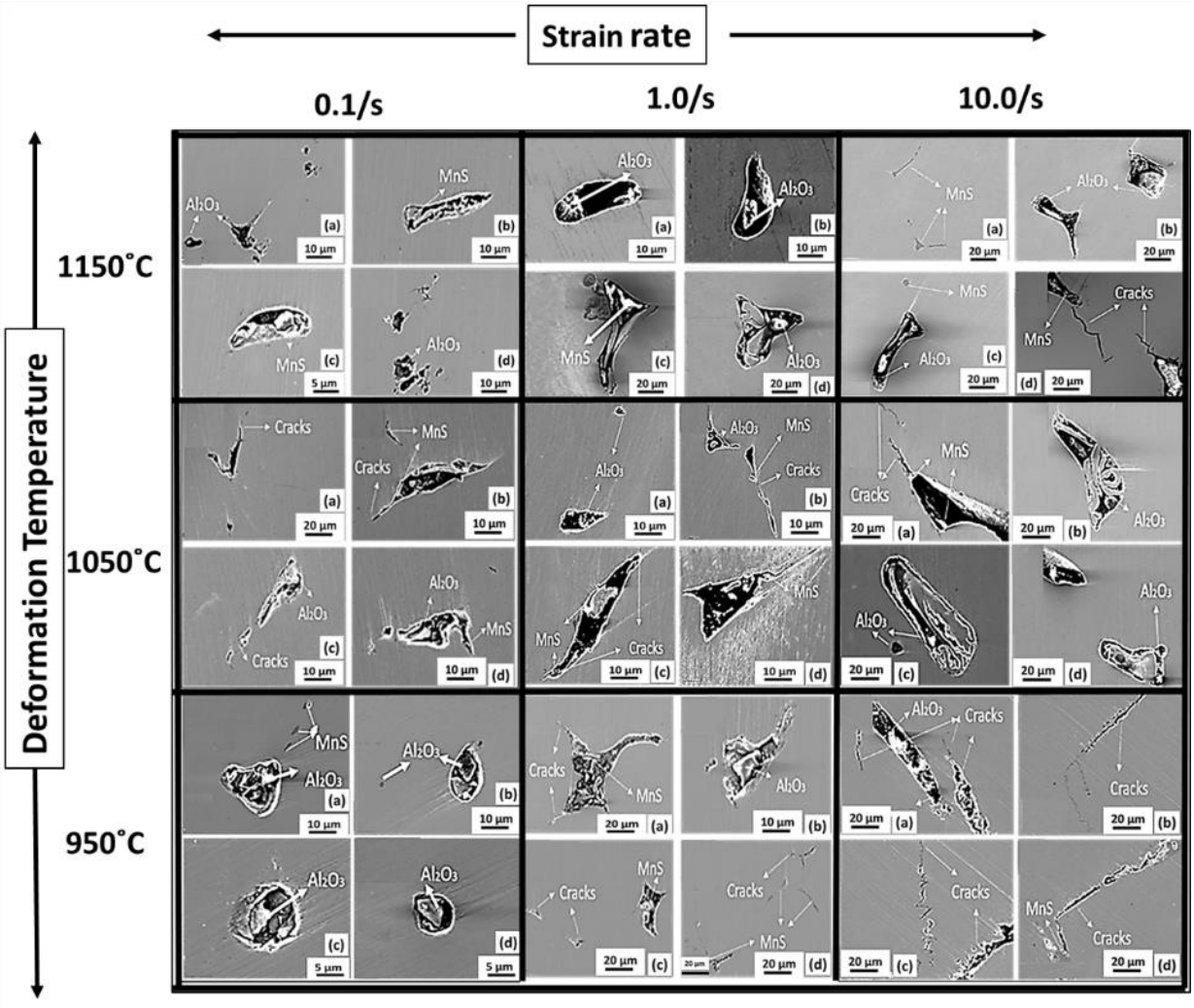
Strain rate
0.1/s
1.0/s
10.0/s
Deformation Temperature
1150˚C
1050˚C
950˚C
Al2O3
MnS
Cracks

TABLE 1

Elements	**C**	**Mn**	**Si**	**S**	**P**	**Cr**	**Ni**	**Mo**	**Al**	**Ca**
Wt. %	0.29	0.488	0.24	0.009	0.015	1.26	4.2	0.25	0.013	0.0015

TABLE 2

Temperature (˚C) - strain rate (/s)	σ_c	σ_s	σ_{ss}	σ_{WH}	σ	X_{DRX}	σ_{WH}	σ	X_{DRX}	σ_{WH}	σ	X_{DRX}
	MPa	MPa	MPa	MPa	MPa	%	MPa	MPa	%	MPa	MPa	%
				0.4 true strain			**0.6 true strain**			**0.8 true strain**		
950-0.1	111	141	109	132	120	36	134	112	70	137	110	82
1050-0.1	70	102	69	93	767	47	95	70	75	98	69	88
1150-0.1	52	67	55	64	56	68	66	57	75	68	57	92
950-1.0	144	172	162	168	162	25	168	162	67	171	165	52
1050-1.0	107	136	123	127	123	33	130	121	69	129	124	70
1150-1.0	75	97	84	93	87	46	94	83	82	95	85	79
950-10.0	168	210	196	207	206	8	207	204	19	208	205	24
1050-10.0	144	165	157	160	159	19	162	159	31	163	158	64
1150-10.0	100	135	117	127	121	34	129	121	44	131	117	78